

Phase Separation Inside the CdTe–CdSe Type II Quantum Dots Revealed by Synchrotron X-ray Diffraction and Scattering

Hwo-Shuenn Sheu,^{*,†} U-Ser Jeng,^{*,†} Wei-Ju Shih,^{*,†} Ying-Huang Lai,^{†,§} Chiu-Hun Su,[†] Chih-Wei Lai,[‡] Meng-Ju Yang,[‡] Yu-Chun Chen,[‡] and Pi-Tai Chou^{*,‡}

National Synchrotron Radiation Research Center, Hsinchu 30076, Taiwan, Department of Chemistry, National Taiwan University, Taipei 106, Taiwan, and Department of Chemistry, Tunghai University, Taichung, 407, Taiwan

Received: February 16, 2008; Revised Manuscript Received: April 14, 2008

Using synchrotron powder X-ray diffraction (PXRD) and small-angle X-ray scattering (SAXS), we have studied the structures of the two CdSe/CdTe and CdTe/CdSe type II quantum dots (QDs), including the crystalline structure, particle shape and size, as well as phase separation of the two components. The X-ray results suggest that the spherical CdTe/CdSe QDs of the size ~ 8 nm, synthesized in a two-step procedure with CdTe nanoparticles (4 nm) as nuclides, have the structure of a CdTe-rich core enclosed by a CdSe shell. On the other hand, the spherical CdSe/CdTe QDs of the size ~ 9 nm, synthesized via a similar two-step procedure but with CdSe nanoparticles (~ 3 nm) as nuclides, show mainly one-phase structure with a relatively uniform distribution of CdSe and CdTe. The phase separation of the two components CdSe and CdTe inside each of the two QDs, a decisive factor in the photovoltaic applications, is furthermore examined using anomalous SAXS (ASAXS) for a consistent conclusion. For comparison, single-phase nanoparticles CdSe and CdTe are also examined. The correlation between the synthesis procedures and the corresponding structures of the QDs is discussed.

1. Introduction

Recently, quite a few type-I and type-II quantum dots (QDs), such as CdSe/ZnS,^{1–4} CdTe/CdSe,^{5–8} CdSe/CdTe,^{9,10} CdSe/ZnTe,¹¹ CdSe/ZnTe/ZnS,¹² CdSe/CdTe/ZnTe,¹⁰ and CdSe/CdS/Zn_{0.5}Cd_{0.5}S/ZnS,¹³ have been synthesized and demonstrated for their potential applications. For type-I QDs, the energy of the conduction band of the shell (the higher band gap material) is higher than that of the core (the lower band gap material) and the energy of the valence band of the shell is lower than that of the core. As a consequence, both electrons and holes are confined in the cores. In contrast, type-II QDs have both valence and conduction bands in the core either lower or higher (in energy) than those in the shell materials.^{5,7} With the characteristic core–shell or core–shell–shell structure to strategically extend the life span of the charge separation by floating electrons or holes onto the outmost shell region, type-II QDs have photophysical properties characteristically differing from those of type-I QDs, and are versatile in many applications in, for instance, electronics, optics, biosensors, imaging, as well as catalysts in redox reactions.¹⁴ As mentioned in the literature,^{1–12} the core–shell-based structures of type-II QDs critically rely on their synthesis processes, and are often examined with traditional powder X-ray diffraction (PXRD), TEM, and EDEX. Despite the many studies devoted to the synthesis procedures and photophysical properties, the core–shell-based structures

of type-II QDs were mainly evidenced from the changes in size and composition rather than the phase separation of the components, due to the limitations in the measuring methodology used.^{1–13,15}

Among the tools involved in the structural characterization of type-II QDs, PXRD can easily identify the crystalline structure and crystalline size of the QDs; the PXRD result, however, cannot correlate straightforward to the phase separation of the components in the QDs of a core–shell structure, especially when the shell is too thin to have a crystalline phase. TEM can identify clearly the shape and size of QDs; nevertheless, TEM images illustrating a clear core–shell structure were rarely reported, due likely to a blurred projection of the thin shell (about 1 or 2 nm) and the low electron density contrast between the core and shell phases (for instance, $1.49 \text{ e}^-/\text{\AA}^3$ for CdTe and $1.43 \text{ e}^-/\text{\AA}^3$ for CdSe in the CdSe–CdTe-based type-II QDs). On the other hand, EDEX, with a capability to identify composition, cannot identify how the component atoms distribute inside a QD.

As demonstrated in several studies,^{16–18} the phase separation of the components of bimetallic catalysts into a core–shell structure can be directly revealed from anomalous small-angle X-ray scattering (ASAXS) and anomalous XRD (AXRD), based on synchrotron X-ray sources of characteristic high photon flux and tunable energy. With X-ray energy tuned close to the absorption edge of a specific element inside nanoparticles (NPs) for PXRD or small-angle X-ray scattering (SAXS), the X-ray scattering cross section of the resonant atoms can be reduced because of the anomalous dispersion of the atoms, resulting in a change in the scattering contrast between the resonant atoms and their environment. The intensity and/or intensity distribution of the AXRD/ASAXS thus changed directly in relation to the positions and distributions of the resonant (highlighted) atoms inside NPs or QDs.^{16–18} In this report, with synchrotron-based

* Author email addresses: hsheu@nsrc.org.tw; usjeng@nsrc.org.tw; chop@ntu.edu.tw.

[†] National Synchrotron Radiation Research Center, National Synchrotron Radiation Research Center, 101, Hsinann Road, Hsinchu 300, Taiwan.

[‡] National Taiwan University, Department of Chemistry, National Taiwan University, 1, Section 4, Roosevelt Road, Taipei 106, Taiwan.

[§] Department of Chemistry, Tunghai University, 181 Section 3, Taichung Harbor Road, Taichung, 407 Taiwan, Telephone and fax numbers: 011-886-2-33663894. E-mail: chop@ntu.edu.tw.

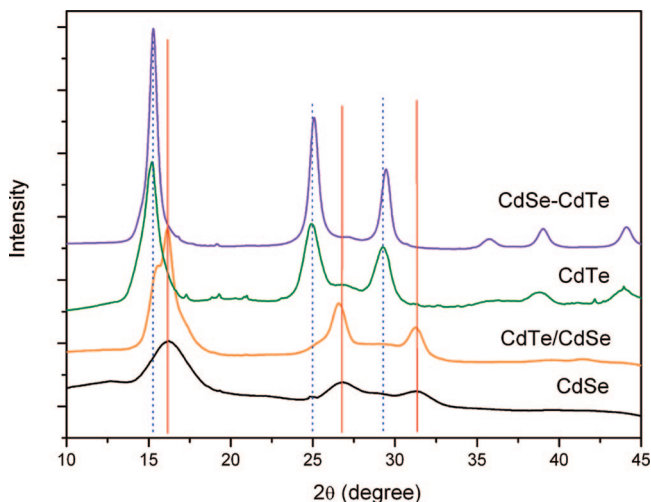


Figure 1. The PXRD patterns of the QDs of CdSe, CdTe, CdSe/CdTe, and CdTe/CdSe. The three red solid lines mark the peak positions of the reflections of CdSe QDs, whereas the three blue dotted lines mark the peak positions of the reflections of the CdTe QDs. The several small peaks in these spectra are due to sample impurity (residual salts after sample purification).

PXRD and SAXS, we have studied the structural characteristics, including crystalline structure, size, shape, and phase separation of the components, of two type-II quantum dots of CdSe/CdTe and CdTe/CdSe, synthesized, respectively, with CdSe and CdTe nuclides in a two-step procedure.

2. Results and Discussion

2.1. PXRD Results. Shown in Figure 1 are the PXRD patterns of the two type-II QDs of CdSe/CdTe and CdTe/CdSe, compared to that of the two single-phase nanoparticles of CdSe and CdTe. The PXRD profile of CdSe NPs can be characterized mainly by a hexagonal phase $P6_3mc$, with lattice constants of $a = b = 4.298$ (3) and $c = 6.981$ (8) Å, together with a minor phase of cubic $F-43m$ of a lattice constant $a = 6.086$ (2) Å. A mean grain size of 2.3 nm of the main $P6_3mc$ phase is extracted from the peak widths using Scherrer's equation. CdSe NPs are known to prefer a Wurtzite structure (hexagonal phase) when the size is smaller than a few nanometers; the preference changes to a cubic phase when the size grows larger.^{19–21} Both the hexagonal and cubic phases of CdSe NPs have four coordinates, but the former has two different bond-distances whereas the latter has only one. In our case, we use the Rietveld refinement method to analyze the PXRD data of the CdSe NPs of the size ~ 3 nm. The result suggests that, in this transition size, the hexagonal phase (68%) and cubic phase (32%) can coexist in the CdSe NPs. The crystalline parameters fitted are shown in Table 1.

On the other hand, the PXRD data of CdTe NPs reveal a crystalline structure in a cubic phase $F-43m$, with $a = 6.5085$ (7) Å and a grain size of ~ 4.9 nm. The two well-separated PXRD patterns of CdSe and CdTe (see Figure 1) serve as a good reference for the structure characterization of the CdSe/CdTe and CdTe/CdSe type-II QDs, since the two nanoparticles are used as nuclides in the syntheses of the two type-II QDs.

For the CdTe/CdSe QDs synthesized with the adsorption of Cd and Se atoms onto CdTe nuclides (~ 4.9 nm), the PXRD result (Figure 1) exhibits a dominant crystalline structure of CdSe. Nevertheless, a shoulder peak near $2\theta = 16^\circ$, a signature of the CdTe crystalline structure, is discernible, revealing the coexistence of CdTe and CdSe crystalline structures. The much

smaller second and third peaks of the CdTe crystalline reflections, compared to that of CdSe, indicate a smaller phase-separated CdTe domain. The result suggests that the CdTe/CdSe QDs consist of a dominant crystalline structure of CdSe and a small CdTe crystalline phase. The Rietveld refinement procedure is used to deconvolute the PXRD data of the CdTe/CdSe QDs (Figure 2), with the following two sets of crystalline phases: (1) the CdTe phase, $F-43m$ crystalline with $a = 6.478(2)$ Å and a crystalline domain size of 4.7 nm, and (2) the CdSe phase, $F-43m$ crystalline with $a = 6.1202(8)$ Å and a crystalline domain size of 4.6 nm. The fitted structural parameters are summarized in Table 1. The CdTe crystalline domain size (4.7 nm) of the CdTe/CdSe QDs is about the same as the CdTe nuclides of 4.9 nm, implying that the CdTe nuclides can survive as a core during the formation of the CdSe shell. Furthermore, according to Vegard's law, the lattice constant $a = 6.120$ Å of the major CdSe phase of the CdTe/CdSe QDs shifts from the 6.086 Å of the pure CdSe NPs, indicating that there may be $\sim 7.4\%$ of CdTe diffusing into the CdSe shell whereas the CdTe-rich core is mixed with 1.2% CdSe.

In contrast to the CdTe/CdSe QDs, the PXRD pattern of the CdSe/CdTe QDs synthesized with the CdSe nuclides (2–3 nm) is completely dominated by the crystalline reflections of CdTe, with no discernible CdSe crystalline reflections. Furthermore, the observed PXRD peaks shift slightly from that of the single-phase CdTe NPs. The result indicates that the CdSe nuclides may dissolve into the CdTe crystalline phase for a uniform distribution. On the basis of Vegard's law for a solid solution phase of CdSe and CdTe, the shifts of the crystalline peaks correspond to about 9% of CdSe uniformly mixed in the CdTe-dominated crystalline phase, for which the composition is consistent with the volume ratio (9%) of the original CdSe NPs to the CdSe/CdTe QDs (3.4 and 7.7 nm diameter for the former and the latter; see the SAXS results shown below). A reasonable Rietveld refinement of the PXRD data of the CdSe/CdTe QDs can be done with a cubic phase of $CdSe_xTe_{1-x}$, with $a = 6.4492(3)$ Å and $x = 8.0\%$ (see Supporting Information Figure SI 1).

2.2. SAXS Results. For a reference, the SAXS data of the CdSe NPs dissolved in toluene solution (0.25 mg/mL) and in powder form are respectively measured. In solution, the NPs can be dispersed relatively well (no interference peak observed), and the corresponding SAXS data can be well-fitted using a sphere form factor with a mean size of 3.4 nm and a Schultz size distribution of 10% (see Figure SI 2a, Supporting Information). The SAXS data measured for the power CdSe NPs exhibit a clear particle–particle interference peak (Supporting Information Figure SI 2b), and the interparticle spacing L of the NPs, ~ 6.3 nm, extracted from the first peak position Q_c (using $L = 7.884/Q_c$),²² indicates that the NPs are surrounded by a surfactant layer of thickness ~ 1.4 nm. Note, due to the low electron density of the surfactants, compared to the NPs, SAXS is mainly sensitive to the size of NPs and their interspacing. On the other hand, the SAXS data of the CdTe NPs (Supporting Information Figure SI 2c) can be fitted with spheres with a diameter of 4.2 nm and a larger polydispersity of 20%, compared to the 10% of CdSe. From the first interference peak at $Q_c = 0.096$ Å⁻¹, we have estimated a mean spacing of 8.2 nm for the CdTe NPs, corresponding a slighter thicker surfactant layer of 2.0 nm. The particle sizes obtained from SAXS for the two NPs are about the same as the crystalline size from the PXRD results (see Table 1), implying that these NPs are of a nearly fully crystalline entity.

TABLE 1: Structural Parameters of the CdSe, CdTe, CdSe/CdTe, and CdTe/CdSe QDs

QDs	space group	cell dimensions (Å)	crystalline grain size (nm) (PXRD)	particle size (nm) (SAXS)
CdSe	$P6_3mc$ (68%)	$a = 4.298(3)$	2.3	3.4 ± 0.3 ($p = 10\%$) ^a
	$F-43m$ (32%)	$c = 6.981(8)$	2.9	
CdTe	$F-43m$	$a = 6.086(3)$	4.9	4.2 ± 0.4 ($p = 20\%$)
CdSe/CdTe	$F-43m$	$a = 6.4492(3)$	7.4	9 ± 0.5 ($p = 12\%$)
CdTe/CdSe	$F-43m$ (core)	$a = 6.457(2)$	4.7	7.7 ± 0.8 ($p = 45\%$)
	$F-43m$ (shell)	$a = 6.1174(6)$	4.6	

^a p is the size polydispersity of the QDs obtained from the SAXS data.

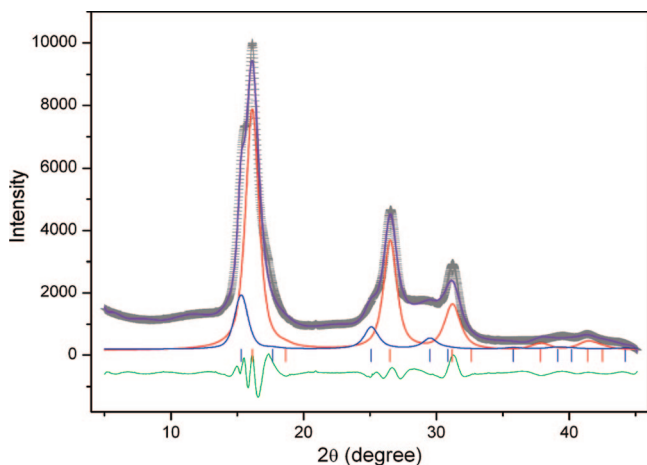


Figure 2. A Rietveld refinement result (purple curve) of the PXRD data of the CdTe/CdSe QDs (daggers), using the two cubic phases of CdTe (blue curve) and CdSe NPs (red curve). The green curve below illustrates the differences between data and simulation, whereas the short sticks mark the reflection positions of the cubic phases of the CdTe and CdSe NPs. The fitted wRp and Rp are 0.0638 and 0.0467, respectively.

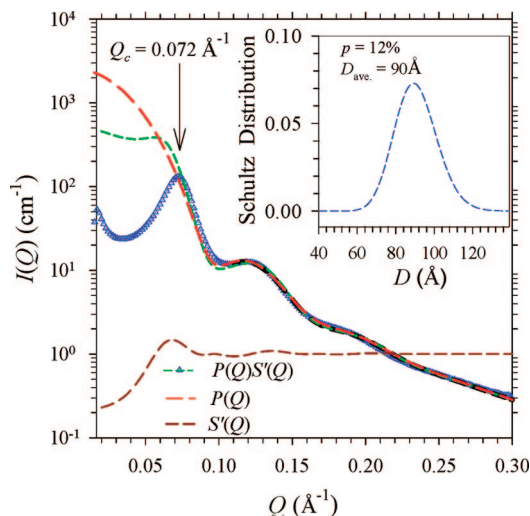


Figure 3. The SAXS data measured with 12.2 keV X-rays for the CdSe/CdTe QDs are fitted (long dashed curve) with polydisperse spheres in the range $Q > 0.09 \text{ Å}^{-1}$, using the Schultz size distribution in the inset. Also shown are the fitted curves $P(Q)S'(Q)$ and $S'(Q)$, illustrating the contribution of the apparent structure factor $S'(Q)$ on the scattering intensity $I(Q)$.

For the CdSe/CdTe QDs, the SAXS data (Figure 3) show a stronger oscillating behavior, indicating a significantly larger particle size than that of the CdSe NPs (see Supporting Information Figure SI 2c). The mean interparticle spacing L of the QDs extracted from the first interference peak at $Q = 0.072$

Å^{-1} is $\sim 11.0 \text{ nm}$, based on $L = 7.884/Q_c$.²² The data fitting with a structural model of CdSe core and CdTe shell cannot converge. The data, however, can be fitted reasonably in the high- Q region ($\geq 0.09 \text{ Å}^{-1}$) with polydisperse spheres of a single-phase structure (Figure 3); the fitted mean diameter D_{ave} is $9.0 \pm 0.5 \text{ nm}$ and the size dispersity p is 12%, with the assumed Schultz distribution. We have also fitted the data using the so-called decoupling approximation to account for the first interference peak at $Q_c = 0.072 \text{ Å}^{-1}$ by an apparent structure factor $S'(Q)$, which is derived from the Percus–Yevick hard-sphere model and modified for the polydispersity effect.²³ The result shown in Figure 3 indicates that the $S'(Q)$ (with the fitted $D_{\text{ave}} = 9.0 \text{ nm}$ and $p = 13\%$) describes only qualitatively the observed interference peak. Likely, the packing density is not uniform in the powder sample, which is not accounted for in the approximation used. Nevertheless, the $S'(Q)$ shown in Figure 3 indicates that the structure factor is close to unity after $Q \geq 0.09 \text{ Å}^{-1}$, in which region the scattering intensity is dominated by the form factor $P(Q)$ of the polydisperse spheres. Based on these results, we neglect the structure factor for simplicity and fit all the SAXS data shown below, in the high Q -region, with solely the form factor $P(Q)$ for polydisperse spheres. The thus obtained structural parameters of the QDs, regarding size and size distribution, are, nevertheless, consistent with that extracted from the corresponding TEM images (see Supporting Information Figure SI 3).

Furthermore, we have examined the structure of CdSe/CdTe QDs with ASAXS. The ASAXS data measured for the CdSe/CdTe QDs with the several X-ray energies of $E = 12.4, 12.55, 12.625, \text{ and } 12.65 \text{ keV}$ overlap rather well, revealing a consistent result of little or no CdSe cores. We keep the X-ray energies below the K-edge absorption energy of Se, 12.658 keV, to avoid provoking fluorescence that would significantly contribute to the scattering background. If the CdSe nuclides kept the integrity as cores in the CdSe/CdTe QDs, we should have observed ASAXS dispersion effects in the high- Q region ($Q > 0.15 \text{ Å}^{-1}$), as that observed for the single-phase CdSe NPs (Figure 4a), since in this region, the scattering is dominated by the core structure of a smaller length scale (3.4 nm) rather than the overall size of the QDs (9 nm). Shown in Figure 4b are the ASAXS profiles for the CdSe NPs, which illustrate the systematical decrease in intensity as the X-ray energy approaches the K-edge absorption of Se at 12.658 keV, due to the drop of the scattering length density of Se (of the CdSe NPs) (see eq 1). For demonstrative purposes, we have calculated the ASAXS profiles at 10 and 12.65 keV for a notional case of a CdSe core (3 nm) and CdTe shell (2.5 nm). The ASAXS profile at 12.65 keV exhibits an intensity drop in the high- Q region and an intensity increase in the intermediate- Q region near 0.13 Å^{-1} . These effects correspond to an enhanced interference between the core and shell structures, due to the drop of the core

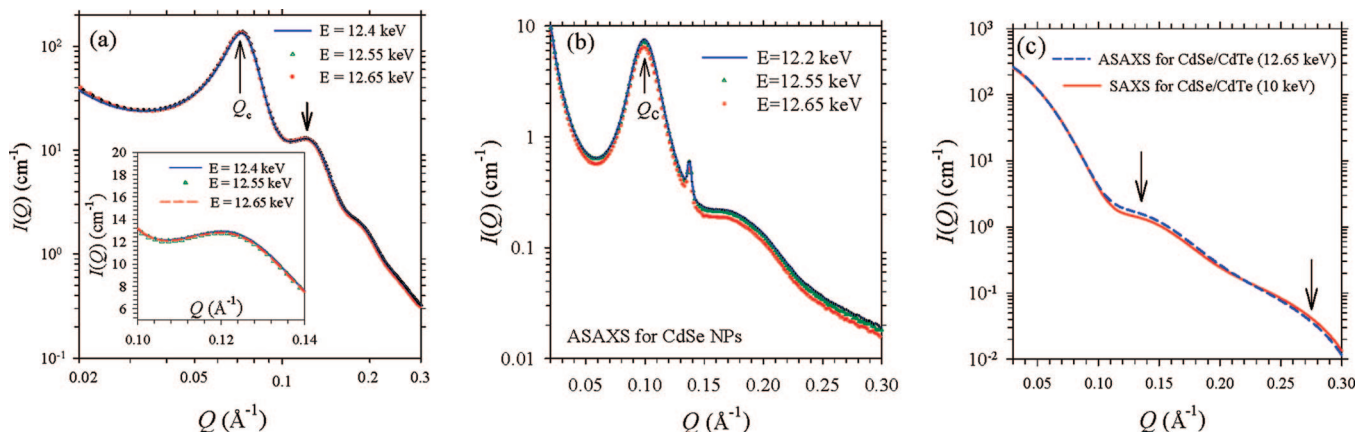


Figure 4. ASAXS data for the CdSe/CdTe QDs in (a) with an enlarged view in the inset, and ASAXS data for the CdSe NPs in (b). Note, the small sharp peak at $Q = 0.13 \text{ \AA}^{-1}$ is contributed by sample impurity. For demonstrative purposes, shown in (c) are the calculated ASAXS profiles at $E = 10$ and 12.65 keV for a notional QD of a CdSe core (3 nm diameter) and a CdTe shell (2.5 nm in thickness), illustrating the differentiable scattering features (indicated by arrows) due to the anomalous dispersion of the phase-separated Se distributed in the QD core.

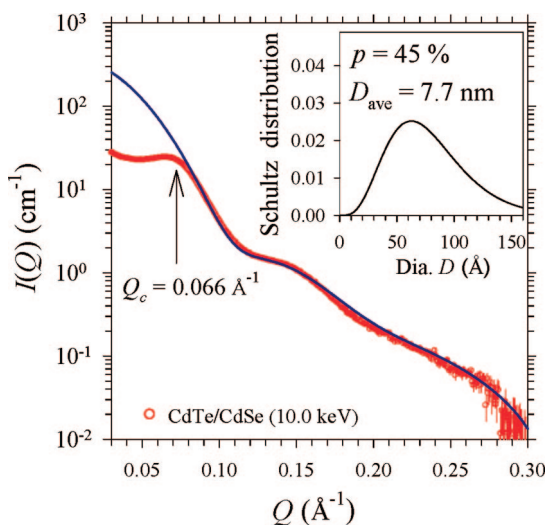


Figure 5. SAXS data for the CdTe/CdSe QDs measured at 10.0 keV . The data are fitted, in the Q -range $> 0.09 \text{ \AA}^{-1}$, with core-shell spheres (solid curve) of a global size distribution shown in the inset.

scattering length density. Numerically, at 10 keV , the difference of the scattering length densities of CdSe ($39.7 \times 10^{-6} \text{ \AA}^{-2}$) and CdTe ($40.5 \times 10^{-6} \text{ \AA}^{-2}$) is $0.8 \times 10^{-6} \text{ \AA}^{-2}$. At $E = 12.65 \text{ keV}$ near the K-edge absorption of Se, the difference is enlarged to $2.7 \times 10^{-6} \text{ \AA}^{-2}$, due to the drop of the scattering length density of CdSe ($37.0 \times 10^{-6} \text{ \AA}^{-2}$). Nevertheless, as shown in Figure 4a, no noticeable scattering enhancement near $Q = 0.13 \text{ \AA}^{-1}$ due to the core-shell interference can be observed in the ASAXS data.

Both the adequate SAXS data fitting with single-phase spheres and the ASAXS data of no changes in the scattering profiles indicate little evidence of a CdSe-core-CdTe-shell structure for the CdSe/CdTe QDs. Likely, the $\sim 9\%$ CdSe in the CdSe/CdTe QDs (estimated from the nuclide size, 3.4 nm , of the CdSe NPs and the size of the CdSe/CdTe, 9 nm) dissolves uniformly in the CdSe/CdTe phase of the QDs, leading to the solid solution crystalline phase of CdSe and CdTe suggested by the previous PXRD result.

Shown in Figure 5 are the SAXS data measured for the CdTe/CdSe QDs, with the first interference peak at $Q_c = 0.066 \text{ \AA}^{-1}$ corresponding to a mean particle spacing $L = 11.9 \pm 0.5 \text{ nm}$. The data in the higher Q region ($Q > 0.09 \text{ \AA}^{-1}$), which are less affected by the interference effect of the QDs, can be adequately

fitted with polydisperse spheres with a core-shell structure. For simplicity, we have defined the polydispersity for the overall size of the QDs, which is a lump sum of the polydisperse core and the polydisperse shell. The core diameter and shell thickness obtained from the fitting are, respectively, $3.0 \pm 0.3 \text{ nm}$ and $2.35 \pm 0.2 \text{ nm}$; the polydispersity 45% obtained for the overall size of the QDs is significantly increased from that of the single-phase CdTe nuclides (20%). The size and size distribution of the CdTe/CdSe QDs obtained match closely with that extracted from the corresponding TEM image (see Supporting Information Figure SI 4).

The core-shell structure of the CdTe/CdSe QDs is further examined using ASAXS. With the X-ray energy tuned close to the K-edge absorption of Se, the scattering length density of the shell dominated by the Se atoms is expected to be suppressed, leading to a lower scattering contrast between the air and shell. Based on the core-shell structural parameters fitted previously with the 10 keV SAXS data, Figure 6a shows the featured profile changes, when the X-ray energy is changed from 10.0 keV to 12.6 and 12.65 keV , near the K-edge absorption of Se. In Figure 6b, the ASAXS data measured at 12.6 keV demonstrate the expected feature changes. Fixing all the structural parameters to that obtained from the 10 keV SAXS data, except the scattering length density of the CdSe shell ($\rho_s = 39.7 \times 10^{-6} \text{ \AA}^{-2}$ at 10 keV), we can fit the 12.6 keV ASAXS data decently with $\rho_s = 38.4 \times 10^{-6} \text{ \AA}^{-2}$, a value slightly larger than the $38.0 \times 10^{-6} \text{ \AA}^{-2}$ for CdSe at 12.6 keV . We attribute this difference to the diffusion of CdTe, $\sim 15 \pm 5\%$, into the CdSe-dominated shell region, resulting in a slightly higher ρ_s due to the higher $\rho_{\text{CdTe}} = 40.52 \times 10^{-6} \text{ \AA}^{-2}$.

In summary, the X-ray diffraction and scattering results suggest that the crystalline CdSe and CdTe phases are well-separated into a core-shell structure inside the CdTe/CdSe QDs. Conversely, the CdSe/CdTe QDs, of a CdTe cubic crystalline structure mainly, can be regarded as a single phase (solid solution) of uniformly distributed CdSe and CdTe; namely, CdSe/CdTe QDs render a uniform distribution of $\text{CdSe}_x\text{Te}_{1-x}$. The alloy-like structure of $\text{CdSe}_x\text{Te}_{1-x}$ -based QDs was also found in several occasions,^{24–26} based on techniques such as PXRD and NMR.²⁴ It seems that CdSe NPs have difficulty maintaining the same crystalline structure in the syntheses for type-II QDs. From our viewpoint, one possible mechanism may lie in the difference of melting point between CdSe and CdTe QDs. We have thus examined the as-prepared CdSe and CdTe nanoparticles with thermal gravimetric analysis (TGA). Interestingly,

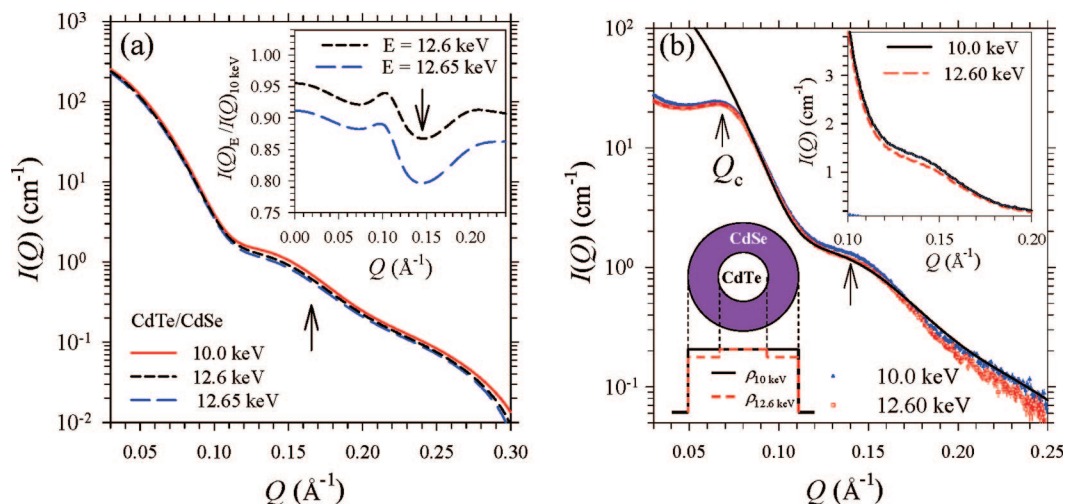


Figure 6. (a) Simulated SAXS profiles for the CdTe/CdSe QDs, with $E = 10, 12.6,$ and 12.65 keV, based on the core–shell structure used in Figure 5. The insets are the SAXS profiles (12.6 and 12.65 keV) normalized to the intensity profile measured at $E = 10$ keV. The arrow indicates the Q -region ($\sim 0.14 \text{ \AA}^{-1}$) where the profile change is most prominent. (b) ASAXS data of the CdTe/CdSe QDs measured at 12.6 keV are compared to the SAXS data measured at 10.0 keV. The inset emphasizes the SAXS intensity changes due to the anomalous dispersion of Se in the CdTe/CdSe QDs. The ASAXS data measured at 12.6 keV are fitted, in the Q -range $> 0.09 \text{ \AA}^{-1}$, with polydisperse spheres (solid curve) of the core–shell structure illustrated by the cartoon.

weight loss of surfactants in CdSe or CdTe nanoparticles based on TGA was rarely reported.²⁷ Our result shown in Supporting Information Figure SI 4 indicates that the surfactant decomposition temperature of CdTe (523 K) is higher than that of CdSe (508 K). Likely, the surface of CdSe nanoparticles might be less protected by the surfactants, when the coating with the CdTe shell layer was proceeded at the temperature of ~ 473 K. This surfactant depleting effect at the temperature near the surfactant decomposition temperature of the CdSe NPs might have created an opportunity for cadmium and tellurium atoms to diffuse deeper into the CdSe nuclides. Similar temperature-dependent diffusion of Te into a CdS layer was also observed in a thin film system using X-ray reflectivity.²⁸ Nevertheless, at this stage, the mechanism for the disappearance of the signature CdSe PXRD pattern in the CdSe-core-based QDs has not been resolved in detail.

3. Conclusions

As elaborated above, using PXRD, SAXS, and ASAXS, we have characterized the structures of the CdSe/CdTe and CdTe/CdSe type-II QDs, synthesized with CdSe and CdTe NPs as nuclides, respectively. We have discussed the correlation between the synthesis procedures and the structure of the quantum dots. The proposed method can be very practical in analyzing the phase separation of type-II quantum dots, and be complementary to other traditional imaging methods, e.g., TEM. As for future work, on one hand, it will be interesting to examine in situ the intermediate structures of CdSe/CdTe QDs in solution during the two-step synthesis with ASAXS. The intermediate structure may provide some more information on the structural evolution of CdSe nuclides in the synthesis procedure. On the other hand, whether the CdSe-core-based, phase-separated type-II QDs can be made via the bottom-up synthetic process remains a great challenge.

4. Experimental Section

4.1. Chemicals. Tri-*n*-octylphosphine oxide (TOPO, 99%, Aldrich), tri-*n*-butylphosphine (TBP, technical grade 98%, SHOWA), di-*n*-octylamine (DOA, 98%, ACROS), hexadecylamine (HDA, 90%, TCI), CdO (99.99%, Strem), selenium (Se)

powder (99.5%, 200 mesh, Aldrich), CdCl₂ (99.99%, Aldrich), tellurium (Te) powder (99.8%, 200 mesh, Aldrich), and zinc stearate (RiedeldeHaDn) were used without further purification.

4.2. Sample Preparation. CdSe/CdTe and CdTe/CdSe QDs in powder form were prepared separately by using the two-step procedure reported previously.^{2–10,29} For CdSe/CdTe QDs, the as-prepared CdSe NPs (0.020 g), TOPO (2.20 g), and HDA (1.26 g) were added in a three-neck flask (50 mL) and heated to 463 K. Meanwhile, CdCl₂ stearate (0.095 g) was dissolved in 2.5 mL TBP upon gentle heating (ca. 353 K). The thus-formed solution of 0.2 M CdCl₂/TBP, after cooling to room temperature, was mixed into a solution of 0.2 M Te/TBP (2.5 mL). Using a syringe pump, the mixture containing Cd and Te ions was furthermore injected into the previous three-neck flask, and the CdSe NPs (core) heated at 468 ± 5 K for 1 h; the final solution in the flask was furthermore annealed at 463 K for 1–1.5 h to yield the final CdSe/CdTe QDs. Centrifugation and reprecipitation were performed twice in methanol for product purification. The synthesis of CdTe/CdSe QDs followed the same procedures used for the CdSe/CdTe QDs.

4.3. Measurements. Powder X-ray diffraction was performed at the BL01C2 beamline of the National Synchrotron Radiation Research Center (NSRRC), with the wavelength λ of 0.9918 Å (12.5 keV). Two-dimensional diffraction patterns were recorded by a Mar345 imaging plate system, with a sample-to-detector distance of 300 mm. Diffraction angle θ was calibrated with Si powders (NBS640b) and silver behenate. One-dimensional XRD profiles were integrated from selected fan-like areas of the symmetrical 2D powder rings using the Fit2D program.³⁰ Crystal structure parameters were refined with the Rietveld method³¹ using the GSAS program,³² and the crystalline grain sizes were obtained from the commonly used Scherrer's equation $d = k\lambda / (B \cos \theta)$, with the crystal grain size d , shape correction constant $k = 0.95$ for spherical particles, and fwhm of the related Bragg peaks B .³³

SAXS data were collected with the SWAXS instrument at the BL17B3 beamline of the NSRRC, with 10.0 keV X-rays for SAXS and several energies near the Se K-edge absorption energy (12.658 keV) for ASAXS. One-dimensional SAXS profiles $I(Q)$ were circularly averaged from 2D images obtained

using a multiwire area detector (gas-type). The scattering wavevector Q , $4\pi \sin(\theta)/\lambda$, defined by the scattering angle 2θ and wavelength λ , was calibrated with silver behenate; the scattering intensity was calibrated to the absolute intensity scale with a polyethylene sample,³⁴ in each energy used for ASAXS. To differentiate small variations in ASAXS, rigorous data corrections for electronic noise of the detector, background scattering, incoming flux, path length of X-rays in the sample, as well as detector pixel sensitivity, were performed, as detailed in our previous report.³⁴

For single-phase polydisperse nanoparticles, SAXS intensity

$$I(Q) \sim S(Q) \int P(Q, r)g(r)dr \quad (1)$$

is described by the structure factor $S(Q)$, the form factor $P(Q) = |F(Q)|^2$, and the probability $g(r) dr$ of the nanoparticles having a size between r and $r + dr$. The particle size distribution function $g(r)$ can be the often used Schultz distribution.³⁵ For spherical particles, the function $F(Q)$ is defined as $V(\rho - \rho_{\text{air}})(3j_1(Qr)/Qr)$, with V for the particle volume, ρ and ρ_{air} for the scattering length densities of the particles and air, and j_1 for the spherical Bessel function.^{36,37} For particles packed with a liquid-like ordering, the first ordering peak position Q_c of $S(Q)$ reveals approximately the mean spacing of the particles through the relation $L = 7.884/Q_c$.²² In the higher Q region, $S(Q)$ approaches unity and the scattering intensity is dominated by $P(Q)$. For phase-separated type-II QDs of a core-shell structure, the form factor in eq 1 can be replaced by the core-shell form factor expressed as

$$P(Q, r) = [F_1(Q, r_1)(W_1 - W_2(V_1/V_2))/(W_1 + W_2) + F_2(Q, r_2)(W_2 + W_2(V_1/V_2))/(W_1 + W_2)]^2 \quad (2)$$

with the contrast of the scattering length densities of the core and shell $W_1 = \Delta\rho = \rho_c - \rho_s$ and the contrast of shell-air $W_2 = \rho_s - \rho_{\text{air}}$. Here V_1 and V_2 are the volumes of the core and shell, respectively.³⁷ Note that the scattering length density $\rho(E)$ of the core or shell is a function of X-ray energy, and can change significantly at a resonant X-ray energy due to the anomalous dispersion of the resonant atoms. As a consequence, near the resonant (absorption) energy, the SAXS profiles of single-phase NPs drop uniformly in intensity, whereas the SAXS profiles for core-shell QDs, of a nonuniform distribution of the resonant atoms, have nonuniform changes.¹⁶

Acknowledgment. This work was supported by the National Science Council, Taiwan, and the National Synchrotron Radiation Research Center.

Supporting Information Available: Rietveld refinement of the CdSe/CdTe PXRD data with the cubic phase of $\text{CdSe}_x\text{Te}_{1-x}$; SAXS data for the CdSe NPs in toluene and in powder form; SAXS data of CdTe NPs in powder form. TEM images for the CdSe/CdTe and CdTe/CdSe QDs. TGA data of CdSe and CdTe nanoparticles. This material is available free of charge via the Internet at <http://pubs.acs.org>.

References and Notes

(1) Dabbousi, B. O.; Rodriguez-Viejo, J.; Mikulec, F. V.; Heine, J. R.; Mattoussi, H.; Ober, R.; Jensen, K. F.; Bawendi, M. G. *J. Phys. Chem. B* **1997**, *101*, 9463–9475.

- (2) Huang, G. W.; Chen, C. Y.; Wu, K. C.; Ahmed, M. O.; Chou, P. T. *J. Cryst. Growth* **2004**, *265*, 250–259.
- (3) Chen, C. Y.; Cheng, C. T.; Lai, C. W.; Wu, P. W.; Wu, K. C.; Chou, P. T.; Chou, Y. H.; Chiu, H. T. *Chem. Commun.* **2006**, 263–265.
- (4) Chen, C. Y.; Cheng, C. T.; Lai, C. W.; Wu, P. W.; Wu, K. C.; Chou, P. T.; Chou, Y. H.; Chiu, H. T. *Chem. Commun.* **2006**, 263–265.
- (5) Chou, P. T.; Chen, C. Y.; Cheng, C. T.; Pu, S. C.; Wu, K. C.; Cheng, Y. M.; Lai, C. W.; Chou, Y. H.; Chiu, H. T. *ChemPhysChem* **2006**, *7*, 222–228.
- (6) Wang, C. H.; Chen, T. T.; Tan, K. W.; Chen, Y. F.; Cheng, C. T.; Chou, P. T. *J. Appl. Phys.* **2006**, *99*, 123521.
- (7) Kim, S.; Fisher, B.; Eisler, H. J.; Bawendi, M. G. *J. Am. Chem. Soc.* **2003**, *125*, 11466–11467.
- (8) Yu, K.; Zaman, B.; Romanova, S.; Wang, D. S.; Ripmeester, J. A. *2005*, *1*, 332–338.
- (9) Blackman, B.; Battaglia, D. M.; Mishima, T. D.; Johnson, M. B.; Peng, X. G. *Chem. Mater.* **2007**, *19*, 3815–3821.
- (10) Chen, C. Y.; Cheng, C. T.; Lai, C. W.; Hu, Y. H.; Chou, P. T.; Chou, Y. H.; Chiu, H. T. *Small* **2005**, *1*, 1215–1220.
- (11) Chen, C. Y.; Cheng, C. T.; Yu, J. K.; Pu, S. C.; Cheng, Y. M.; Chou, P. T. *J. Phys. Chem. B* **2004**, *108*, 10687–10691.
- (12) Cheng, C. T.; Chen, C. Y.; Lai, C. W.; Liu, W. H.; Pu, S. C.; Chou, P. T.; Chou, Y. H.; Chiu, H. T. *J. Mater. Chem.* **2005**, *15*, 3409–3414.
- (13) Xie, R. G.; Kolb, U.; Li, J.; Basche, T.; Mews, A. *J. Am. Chem. Soc.* **2005**, *127*, 7480–7488.
- (14) Medintz, I. L.; Uyeda, H. T.; Goldman, E. R.; Mattoussi, H. *Nat. Mater.* **2005**, *4*, 435–446.
- (15) Rogach, A. L.; Kornowski, A.; Gao, M.; Eychmüller, A.; Weller, H. *J. Phys. Chem. B* **1999**, *103*, 3065–3069.
- (16) Jeng, U.; Lai, Y.-H.; Sheu, H.-S.; Lee, J.-F.; Sun, Y.-S.; Chuang, W.-T.; Huang, Y.-S.; Liu, D.-G. *J. Appl. Crystallogr.* **2007**, *40*, s418–s422.
- (17) Haubold, H. G.; Vad, T.; Waldofner, N.; Bonnemann, H. *J. Appl. Crystallogr.* **2003**, *36*, 617–620.
- (18) Brumberger, H.; Hagerman, D.; Goodisman, J.; and Finkelstein, K. D. *J. Appl. Phys.* **2005**, *38*, 147–151.
- (19) Shimojo, F.; Kodiyalam, S.; Ebbsjö, I.; Kalia, R. K.; Nakano, A.; Vashishta, P. *Phys. Rev. B* **2004**, *70*, 184111.
- (20) Jacobs, K.; Wickham, J.; Alivisatos, A. P. *J. Phys. Chem. B* **2002**, *106*, 3759–3762.
- (21) Grünwald, M.; Rabani, E.; Dellago, C. *Phys. Rev. Lett.* **2006**, *96*, 255701–255704.
- (22) Chen, S. H.; Sheu, E. Y.; Kalus, J.; Hoffmann, H. *J. Appl. Crystallogr.* **1988**, *21*, 751–769.
- (23) Kotlarchyk, M.; Chen, S.-H. *J. Chem. Phys.* **1983**, *79*, 2461–2469.
- (24) Ratcliffe, C. I.; Yu, K.; Ripmeester, J. A.; Zaman, M. B.; Badarau, C.; Singh, S. *Phys. Chem. Chem. Phys.* **2006**, *8*, 3510–3519.
- (25) Bailey, R. E.; Nie, S. M. *J. Am. Chem. Soc.* **2003**, *125*, 7100–7106.
- (26) Li, Y. C.; Zhong, H. Z.; Li, R.; Zhou, Y.; Yang, C. H.; Li, Y. F. *Adv. Funct. Mater.* **2006**, *16*, 1705–1716.
- (27) Foos, E. E.; Wilkinson, J.; Makinen, A. J.; Watkins, N. J.; Kafafi, Z. H.; Long, J. P. *Chem. Mater.* **2004**, *18*, 2886–2894.
- (28) Kim, S.; Soo, Y. L.; Kioseoglou, G.; Kao, Y. H.; Compaan, A. D. *J. Appl. Phys.* **2004**, *96*, 1007–1012.
- (29) Peng, X. G.; Schlamp, M. C.; Kadavanich, A. V.; Alivisatos, A. P. *J. Am. Chem. Soc.* **1997**, *119*, 7019–7029.
- (30) Hammersley, A. P. ESRF Internal Report, FIT2D V12.012 Reference Manual V6.0 ESRF98HA01T (2004).
- (31) Rietveld, H. M. *J. Appl. Crystallogr.* **1969**, *2*, 65–71.
- (32) Larson, A. C. and Von Dreele, R. B. General Structure Analysis System (GSAS), Los Alamos National Laboratory Report LAUR86–748, 2000.
- (33) Cullity, B. D. *Elements of X-Ray Diffraction*, 2nd ed.; Addison Wesley Publishing Company: Reading, MA, 1978; pp 99–106.
- (34) Lai, Y. H.; Sun, Y. S.; Jeng, U.; Lin, J. M.; Lin, T. L.; Sheu, H. S.; Huang, W. T.; Huang, Y. S.; Hsu, C. H.; Lee, M. T.; Lee, H. Y.; Liang, K. S.; Gabriel, A.; Koch, M. H. J. *J. Appl. Crystallogr.* **2006**, *39*, 871–877.
- (35) Sheu, E. Y. *Phys. Rev. A* **1992**, *45*, 2428–2437.
- (36) Chen, S. H.; Lin, T. L. *Methods of Experimental Physics - Neutron Scattering in Condensed Matter Research*; Sködl, K., Price, D. L., Eds.; Academic Press: New York, 1987; pp 489–543.
- (37) Lin, T. L.; Chen, S. H.; Gabriel, N. E.; Roberts, M. F. *J. Am. Chem. Soc.* **1986**, *108*, 3499–3507.